Mallor, F., Raiola, M., Sanmiguel Vila, C., Örlü, R., Discetti, S y Ianiro, A. (2019). Modal decomposition of flow fields and convective heat transfer maps: An application to wall-proximity square ribs. *Experimental Thermal and Fluid Science*, 102, pp. 517-527.

DOI: https://doi.org/10.1016/j.expthermflusci.2018.12.023

# Modal decomposition of flow fields and convective heat transfer maps: an application to wall-proximity square ribs

Fermin Mallor[a,b], Marco Raiola[a], Carlos Sanmiguel Vila[a], Ramis Örlü[b], Stefano Discetti[a], Andrea Ianiro[a,*]

[a] *Aerospace Engineering Research Group, Universidad Carlos III de Madrid, Avenida de la Universidad, 30, 28911, Leganes, Spain*
[b] *Linné FLOW Centre, Dept. of Mechanics, KTH Royal Institute of Technology, Stockholm, Sweden*

**Abstract**

In this work a modal decomposition approach to convective heat transfer distributions in turbulent flows is explored. The organization and thermal footprint of the turbulent flow features generated downstream of wall-proximity two-dimensional square ribs immersed in a turbulent boundary layer is investigated experimentally. This study employs modal decomposition to investigate whether this analysis can allow identifying which characteristics of the flow topology are responsible for the Nusselt-number augmentation, aiming to uncover the underlying physics of heat-transfer enhancement. Heat transfer and flow velocity measurements are performed at a Reynolds number (based on the free-stream velocity and rib side-length) equal to 4600. Square ribs are tested for two different gap spacings from the wall (0.25 and 0.5 ribs side-length) and in the wall-attached configuration. A low-thermal-inertia heat transfer sensor coupled with high-repetition-rate IR thermography is designed to study the unsteady variation of the convective heat-transfer coefficient downstream of the obstacles. Flow-field measurements are performed with non-time-resolved Particle Image Velocimetry (PIV). A modal analysis with Proper Orthogonal Decomposition (POD) is applied to both convective heat-transfer maps and velocity-fields. The comparison of the Nusselt-number spatial modes of the clean turbulent boundary layer configuration and of the configurations with the ribs shows a variation of the spatial pattern associated with oscillations with strong spanwise coherence, opposed to the thin elongated streaks which dominate the convective heat transfer in the clean turbulent boundary layer. In configurations where the convective heat transfer is enhanced by coherent structures located close to the wall, similar eigenspectra are observed for both flow field and convective heat transfer modes. The results of the modal analysis support a picture of a direct relation between the coherence of near-wall flow features and heat-transfer augmentation, providing a statistical evidence for the fact that near-wall coherent eddies are extremely efficient in enhancing heat transfer.

*Keywords:* POD, Unsteady turbulent convection, Rib turbulators, Turbulent boundary layers, IR thermography

## 1. Introduction

In several industrial fields (e.g. electronic packaging and turbomachinery) the cooling capabilities have become a technology driving factor (see, e.g. Refs. [1, 2]) due to the need of removing large amounts of heat from compact spaces. The research on heat transfer enhancement approaches has provided in the last decades outstanding advances in strategic technological fields such as, for instance, that of gas turbines [1]. Heat transfer enhancement studies mostly focused on turbulent flows which enable values of the convective heat transfer coefficient among the highest for single-phase flows [3].

During the last five decades, the coherent structures received a large attention from the turbulence community. Modal decomposition approaches, such as Proper Orthogonal Decomposition (POD, [4]), are nowadays a standard for the analysis of turbulent flows and the extraction of the coherent structures.

While it is rather intuitive that the high heat transfer in turbulent flows is strongly connected to the presence of turbulent structures in the flow, the effect of these structures on the instantaneous wall heat transfer is still largely unexplored because, due to the difficulty in designing and manufacturing low-thermal-inertia heat transfer sensors, only very few studies have provided detailed information about the instantaneous convective heat transfer distributions in turbulent problems (see, e.g. Refs. [5, 6, 7, 8]).

Few studies have employed modal analysis for the determination of the role of turbulent features in the scalar transport problem (see, e.g. Refs. [9, 10, 11]). In a recent numerical study Antoranz et al. [9] analyzed the problem of turbulent transport in a pipe with non-homogeneous heating by means of the Extended Proper Orthogonal Decomposition (Extended POD) [12] and identified which flow structures are responsible of the heat transport in such problem. While the approach proposed by Antoranz et al.

*Corresponding author
*Email address:* aianiro@ing.uc3m.es (Andrea Ianiro )

**Nomenclature**

| | | | |
|---|---|---|---|
| $\beta$ | Stefan-Boltzmann constant | $Gr$ | Grashof number |
| $\Delta T$ | Temperature difference | $H$ | Gap height |
| $\delta_{99}$ | Boundary layer thickness | $h$ | Heat-transfer coefficient |
| $\delta_{\text{foil}}$ | Thin foil thickness | $I$ | Current intensity of the power supply |
| $\epsilon$ | Wall emissivity | $k_{\text{air}}$ | Air thermal-conductivity coefficient |
| $\nu$ | Kinematic viscosity | $k_{\text{foil}}$ | Thin foil thermal-conductivity coefficient |
| $\phi_{\text{i}}$ | $i^{\text{th}}$ spatial mode | $L$ | Rib side length |
| $_{\text{i}}$ | $i^{\text{th}}$ temporal mode | $n_{\text{m}}$ | Rank of $\underline{\underline{\mathcal{G}}}$ |
| $\rho$ | Foil density | $n_{\text{p}}$ | Number of grid points |
| $\sigma_{\text{i}}$ | $i^{\text{th}}$ singular value | $n_{\text{s}}$ | Number of snapshots |
| $\underline{\underline{\mathcal{C}}}$ | Temporal correlation matrix | $Nu$ | Nusselt number |
| $\underline{\underline{\mathcal{G}}}$ | Snapshot matrix | $q''_{\text{j}}$ | Joule heating |
| $\underline{\underline{\Phi}}$ | Spatial basis | $Re$ | Reynolds number based on rib side length |
| $\underline{\underline{\Psi}}$ | Temporal basis | $Re_\tau$ | Friction Reynolds number |
| $\underline{\underline{\Sigma}}$ | Singular value matrix | $t$ | Time |
| $A_{\text{foil}}$ | Area of the thin foil | $T_{\text{amb}}$ | Ambient temperature |
| $c$ | Specific heat capacity coefficient | $T_{\text{aw}}$ | Adiabatic wall temperature |
| $E$ | Voltage from power supply | $U_\infty$ | Free-stream velocity |
| $G(\vec{x},t)$ | Generic flow-field quantity | $u_\tau$ | Friction velocity |
| $g(\vec{x},t)$ | Fluctuating part of $G(\vec{x},t)$ | w | Foil surface temperature |

[9] proved to be powerful, it requires the the availability of simultaneous instantaneous flow fields and convective-heat-transfer coefficient (or temperature) maps, provided by either computationally expensive Direct Numerical Simulations (which can not be used for extensive parametric studies) or complex simultaneous synchronized measurements [7] (which might not be feasible in complex setups with reduced optical access).

In the present work, POD is applied to time-resolved convective heat transfer measurements [6, 8] to provide access to a modal decomposition of the wall convective heat transfer coefficient. To the authors knowledge, such analysis has never been attempted before. The availability of convective heat transfer modes raises two interesting questions:

- Can POD modes of wall convective heat transfer maps be a useful tool for the understanding of turbulent heat transfer processes?
- Is there any relation between flow field and convective heat transfer coefficient modes?

It is virtually impossible to provide a general answer to such questions, for all classes of turbulent flows. For this reason, we explore the problem of a rib-roughened wall, which is very appealing due to the extensive availability of experimental datasets and to the richness of flow features involved.

The inclusion of obstacles and roughness elements to enhance transport in boundary layers is common since it provides a twofold advantage, viz. an increased surface area for the convection process and the capability of generating beneficial secondary turbulent-flow structures. The literature about the use of rib roughness elements in channel or pipe flows is extremely wide, with first research works lasting from the seventies [13]. A wide variety of both experimental and computational studies has been performed, making use of countless experimental approaches such as optical methods [14], IR thermography [15, 16] or mass-transfer analogy [17]. The development of computational capabilities has also enabled comprehensive DNS studies (see, e.g. Ref. [18]), while the progress of flow field measurement techniques has allowed for a detailed characterization of the instantaneous turbulent flow organization (see, e.g. Ref. [19]).

Several studies have attempted to relate local heat transfer enhancement with the instantaneous flow organization, often applying a modal decomposition approach to isolate

the most energetic flow features [20, 21] however, modal analyses of instantaneous convective heat transfer distributions are still lacking.

In the case of rib-roughened walls, the convective heat-transfer coefficient downstream of an obstacle is somewhat low, due to the formation of a recirculation region, upon which it increases and decreases again after having reached a maximum [14, 17, 18, 20]. The local minimum of the convective heat-transfer coefficient leads to the formation of hot spots [17, 20, 22, 23]. Attempts to tackle this issue have led to modified designs which are able to improve heat-transfer performances. A suitable option to enhance the performance of spanwise ribs is represented by the use of detached wall-proximity ribs [14], which suppress the near-wall recirculation zone downstream of the rib. In their recent work He et al. [20] report detailed flow-field and heat-transfer measurements by means of Particle Image Velocimetry (PIV) and Temperature Sensitive Paints (TSPs). Their results show that the presence of a gap between the rib and the wall may promote the formation of a wall jet, allowing to remove the hot spot located immediately downstream of the rib. Proper Orthogonal Decomposition (POD) of PIV data is used to visualize the different flow structures in the wake showing that for a rib attached or very close to the wall the dominant feature is represented by a flapping motion of the wake of the rib. Increasing the gap beyond 0.5 rib heights, the dominant feature is, however, that of the vortex shedding from the rib, which behaves similarly to a cylinder in ground effect [24].

The significant richness and complexity of the different configurations of wall-proximity ribs, as identified in Ref. [20], allows to study different turbulent structures by simply changing the gap, from a shedding layer to a Von Kármán vortex street, going through a complex interaction between a near-wall jet with the shedding. This makes the wall-proximity rib extremely suitable for exploring the meaningfulness and usefulness of the convective heat transfer modes.

This work combines PIV [25] and time-resolved convective heat-transfer measurements [8], allowing to identify both flow fields and convective heat transfer coefficient POD modes in the wake of wall-proximity ribs in a turbulent boundary layer (TBL). The convective heat transfer coefficient is here non-dimensionalized in terms of Nusselt number, thus Nusselt number modes are reported. A comparison of these features allows to estimate whether it exists and which is the relationship between the variance of the Nusselt number and the turbulent coherent structures of the flow. The experimental setup and the post-processing strategies are described in Sec. 2. The time-averaged flow-field and heat-transfer distributions are outlined in Sec. 3 to identify the main features of each configuration. The instantaneous flow-field and heat-transfer maps are then post-processed to extract the modal decompositions with POD, as illustrated in Sec. 4, prior to concluding the work in Sec. 5.

## 2. Methodology

### *2.1. Experimental set-up*

The IR thermography and PIV measurements were performed in the Göttingen type wind tunnel of the Aerospace Engineering Group at the Universidad Carlos III de Madrid. The tunnel has a square test section of $0.4 \times 0.4$ m$^2$ and is capable of reaching a maximum speed of 20 m/s. The schematic of the experimental setup is reported in Figure 1. A splitter plate with a thickness of 10 mm was mounted in the test section at a distance of 0.1 m from its back wall. A 2.4 mm-high turbulator strip was placed at a distance of 75 mm from the leading edge in order to fix the transition location and to obtain a fully developed TBL downstream in the measurement section, located 575 mm downstream of the turbulator. It was ensured that the turbulent boundary layer at the measurement location was not affected by tripping effects, i.e. that the clean boundary layer (with no ribs) was not reminiscent of the inflow conditions [26, 27]. In order to characterize the boundary layer parameters, an enhanced-resolution EPTV approach (Ensemble Particle Tracking Velocimetry) [28] is applied in a test with a clean boundary layer. The absolute wall position and the friction velocity have been estimated using the composite profile given in [29] as described in Ref. [30]. The boundary layer thickness $\delta_{99}$ (here defined as the position at which 99% of the free-stream velocity $U_\infty$ is attained) has been determined to be of 42 mm, resulting in a friction Reynolds number approximately equal to 900 ($Re_\tau = u_\tau \delta_{99}/\nu$, where the boundary layer thickness is used as the characteristic length and $\nu$ is the fluid kinematic viscosity) at the location where the ribs were placed.

Square two-dimensional ribs with 10 mm side length $L$ were used in the present study as obstacles due to the simplicity of their geometry. The wall-normal height of the obstacles is equal to approximately a quarter of the local boundary layer thickness ($L/\delta_{99} \approx 0.24$).

The experiments were carried out with the ribs placed at three different wall-normal heights $H$ from the wall: 0, 2.5 mm and 5 mm, corresponding to $H/L = 0$, 0.25 and 0.5, respectively. The gap from the wall was obtained using supports, as indicated in Figure 1b), located at $12L$ from the lateral edges of the foil. Measurements performed in the clean boundary layer are used as a baseline case. Thus, a total of 4 different configurations were analyzed. In all the cases, the velocity of the wind tunnel was set to 7.1 m/s, obtaining a local Reynolds number approximately equal to 4600, based on the free-stream velocity $U_\infty$ and on the rib side length $L$, ($Re = U_\infty L/\nu$). The streamwise turbulence intensity for this free-stream velocity was estimated to be below 0.3%.

### *2.2. Measurement techniques*

The measurement setup and arrangement is similar to that used in Ref. [21]. Flow-field measurements are performed in a streamwise/wall-normal plane with PIV. The

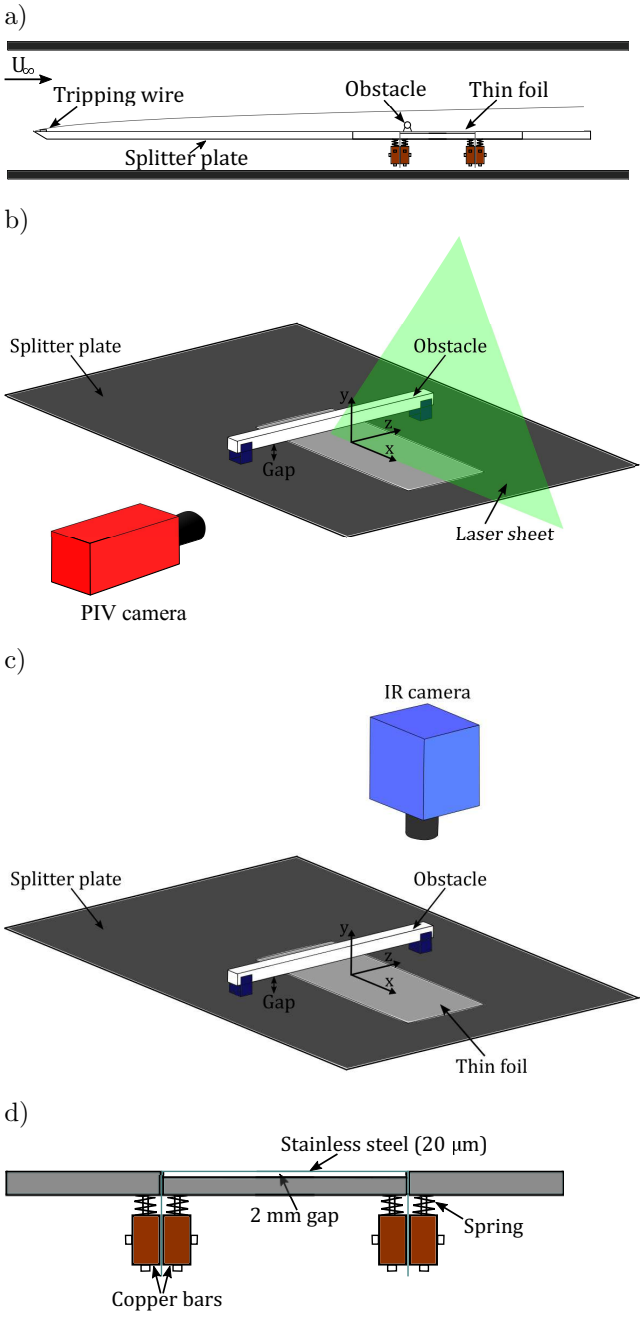


Figure 1: Sketch of the experimental set-up a) Test section arrangement; b) PIV experimental setup; c) Infrared Thermography arrangement; d) Close-up of the thin foil configuration. Subfigures b and c include the obstacle configuration and the coordinate system.

PIV setup arrangement is sketched in Figure 1b). Convective heat transfer measurements on the wall are performed with a heated-thin-foil sensor coupled with IR thermography [31], as illustrated in Figure 1c–d). The main difference with respect to the setup used in Ref. [21] consists in the use of a low-thermal-inertia heat-transfer sensor coupled with a high-repetition-rate IR thermography, in order to enable time-resolved measurements of the convective heat-transfer coefficient [6, 8].

The heat-transfer sensor is made of a stainless steel thin foil (with a thickness of 20 $\mu$m) flash-mounted on the flat plate at a distance of 0.65 m downstream of the leading edge. As mentioned in Ref. [32], the temperature fluctuations on the surface are attenuated both in time and space due to the sensor thermal inertia and conduction. This problem is minimized by use of a 20 $\mu$m thin foil, with a relatively small thermal inertia. The foil is heated with a constant heat flux through the Joule effect by passing through it a current provided by a DC power supply. The Joule heating $q_{\mathrm{j}}''$ is equal to $EI/A_{\mathrm{foil}}$, with $E$ and $I$ being respectively the supplied voltage and current, and $A_{\mathrm{foil}}$ denoting the surface area of the foil. A 2 mm gap is left in between the splitter plate substrate and the thin foil (as sketched in Figure 1d) in order to minimize conduction and natural convection losses through the back-side of the foil.

In order to assure a constant heat flux through the whole surface of the foil, the current is supplied by means of two copper bars attached to each end of the foil, using indium wires to minimize the electrical resistance between the different elements. The electrical power is provided using a stabilized power supply, set to $E \approx 2$ V and $I \approx 15$ A in order to obtain a temperature difference $\Delta T \approx 25$ K between the wall temperature of the heated foil $T_{\mathrm{w}}$ and the adiabatic wall temperature $T_{\mathrm{aw}}$. Compression springs are used in order to assure the flatness of the foil, as well as to add stiffness to it, effectively eliminating any vibrations caused by the flow excitation.

As mentioned before, the presence of a thin air gap between the foil and the plate allows to minimize heat conduction from the back side of the foil. The heat transfer in the front side of the thin foil is dominated by forced convection effects since the relation between buoyancy and inertial forces, given by the ratio of the Grashof number and the squared Reynolds number is much smaller than one ($Gr/Re^2 \ll 1$). The convective heat-transfer coefficient $h$ is estimated from the energy balance through the foil:

$$c\rho\delta_{\mathrm{foil}}\frac{dT_{\mathrm{w}}}{dt} = q_{\mathrm{j}}'' + k_{\mathrm{foil}}\delta_{\mathrm{foil}}\nabla^2 T_{\mathrm{w}} - h(T_{\mathrm{w}} - T_{\mathrm{aw}}) - \epsilon\beta(T_{\mathrm{w}}^4 - T_{\mathrm{amb}}^4) \quad (1)$$

where $c$ is the specific heat-capacity coefficient of steel, $\delta_{\mathrm{foil}}$ the foil thickness, $k_{\mathrm{foil}}$ the foil thermal-conductivity coefficient, $h$ the convective heat-transfer coefficient, $\epsilon$ the wall emissivity, $\beta$ the Stefan-Boltzmann constant.

The temperature at the wall is measured using a FLIR SC4000 InSb IR camera (with a noise equivalent temperature difference equal to 20 mK in the considered measurement range), using a reduced focal plane array ($128 \times 128$ instead of $320 \times 256$ elements) in order to achieve an acquisition rate equal to 1.5 kHz, with a spatial resolution of 16 pixels/$L$. The foil is covered with a thin layer of high emissivity enamel ($\epsilon$=0.98) in order to reduce the uncertainty of temperature measurements performed with the IR camera. The effects of tangential conduction through the foil

($q''_{\rm k} = -k_{\rm foil}\delta_{\rm foil}\nabla^2 {\rm w}$) are neglected in the post-processing of the data, since its maximum contribution was found to be of order 1% of $q''_{\rm j}$ due to the rather low foil thermal conductance [33]. A total of $10^5$ IR images are acquired both with the power source turned on ($T_{\rm w}$) and off ($T_{\rm aw}$). In order to properly capture the convective heat-transfer coefficient fluctuations, the measurement accuracy of the small temperature fluctuations involved in the problem needs to be improved beyond the limit of the IR camera. The optimal POD-based filter developed by Raiola et. al [8] is used to remove random noise fluctuations along with a $2^{nd}$-order polynomial filter over a $7 \times 7 \times 7$ kernel; additionally, a residual 50 Hz spurious term reminiscent of the power supply input current is removed by filtering the signal in the band 49-51 Hz. Using the criterion introduced in Ref. [8], a low-rank reconstruction of the IR camera temperature measurements is performed using approximately the first 200 POD temperature modes (each configuration has its own optimal number of modes).

The values of the convective heat-transfer coefficient $h$ were reduced to non-dimensional form in terms of the Nusselt number ($Nu = hL/k_{\rm air}$).

The flow fields are measured with PIV. The measurements are performed in the streamwise/wall-normal plane at the wind-tunnel symmetry plane. The experimental setup, sketched in Figure 1b) is essentially the same as that described in Ref. [21]. A dual cavity Nd:Yag Quantel Evergreen laser is used in order to illuminate Di-Ethyl-Hexyl-Sebacate seeding particles. The recording device is an Andor sCMOS camera, equipped with a lens with 50 mm focal length and using a relative aperture $f/\#$ equal to 11. Images are recorded with a spatial resolution of 22 pixels/mm. Since the magnification is rather low (approximately 0.14) the errors due to perspective effects are negligible [34]. Sets of 2000 image pairs have been captured at an acquisition rate of 10 Hz for each of the 4 test cases. The raw images are pre-processed to remove the background due to the strong reflections using the POD-based background removal method reported in Ref. [35]. A custom-made PIV software developed at the University of Naples Federico II is used to perform digital cross-correlation analysis of the particle images [36] to calculate the velocity fields. The interrogation strategy is an iterative multi-grid/multi-pass [37] image deformation algorithm [38], with final interrogation windows of $64 \times 64$ pixels with 75% overlap (the final vector spacing is equal to 16 pixels, i.e. 0.72 mm, which results in 14 vectors/$L$). B-spline interpolation schemes are used to improve the accuracy of the PIV processing [39, 40]. The vector validation to identify invalid vectors is carried out with a universal median test [41] on a $5 \times 5$ vectors kernel and an error threshold equal to 2. Discarded vectors (less than 5% of the total vectors) are replaced with a distance-weighted average of neighboring valid vectors (being the weight inversely proportional to the distance from the location of the vector to be corrected, and the kernel of vectors used for the interpolation equal to that used for outlier detection).

Table 1: Table of uncertainties.

| **Parameter** | **Uncertainty** |
|---|---|
| $T_{\rm w} - T_{\rm aw}$ | 0.1 K |
| $T_{\rm amb}$ | 0.1 K |
| $A_{\rm foil}$ | 0.1 % |
| $\delta_{\rm foil}$ | 0.1 % |
| $L$ | 0.1 % |
| $I$ | 0.2 % |
| $E$ | 0.2 % |
| $\epsilon$ | 1 % |
| $k_{\rm air}$ | 0.2 % |
| $k_{\rm foil}$ | 0.2 % |
| $c$ | 0.2 % |
| $\rho$ | 0.2 % |
| $q''_{\rm k}$ | 10 % |

The uncertainty of the local Nusselt number is estimated with the methodology proposed in Ref. [42] using the measurement uncertainties reported in Table 1. The measurement uncertainty for the time averaged Nusselt number was found to be of $\pm 5\%$. The uncertainty estimation for the instantaneous Nusselt number maps is non-trivial. However, Ref. [43] reports uncertainties of about 8% for phase averaged $Nu$ maps; the large number of snapshots used for the present investigation allows to assume a similar uncertainty for the Nusselt-number modes (expecially those with larger variance content). For what concerns the PIV uncertainty, it is quantified to be lower than 1%, while the large number of PIV snapshots suggests a satisfactory convergence of the flow statistics.

### *2.3. POD analysis*

After removing the time-averaged flow field and Nusselt number maps, a POD analysis of the fluctuating part of the instantaneous flow fields and Nusselt-number distributions is carried out in this work. The POD analysis provides orthogonal modes sorted by the Frobenious norm of their contribution to the dataset, i.e. their contribution to the variance, and allows to extract information about the turbulent coherent structures in the wake and about the wall Nusselt-number coherent patterns for the configurations with the rib and to compare them with respect to those in the baseline configuration.

The POD identifies an orthonormal basis for a data matrix using functions estimated as solutions of the integral eigenvalue problem known as Fredholm equation; consequently the POD modes are optimal in the least-square sense [4]. In particular, the snapshot method [44] has been used for the purpose of the present study. In this section, a brief introduction to the Proper Orthogonal Decomposition method will be provided; for further details, refer to Ref. [45].

Any flow quantity $G(\vec{x}, t)$ (e.g. velocity or Nusselt-number distribution in this work), can be decomposed into a time-

averaged ($\overline{G}(\vec{x})$) and fluctuating ($g(\vec{x},t)$) component. The quantity $G(\vec{x},t)$ is measured over $n_\mathrm{p}$ grid points for each of the $n_\mathrm{s}$ snapshots. The fluctuating component $g(\vec{x},t)$ can then be rearranged into the so-called 'snapshot matrix' $\underline{\underline{\mathcal{G}}}$, whose rows are the $n_s$ snapshot vectors. The temporal correlation matrix $\underline{\underline{\mathcal{C}}}$ is computed by multiplying $\underline{\underline{\mathcal{G}}}$ by its transpose $\underline{\underline{\mathcal{G}}}'$:

$$\underline{\underline{\mathcal{C}}} = \underline{\underline{\mathcal{G}}}\,\underline{\underline{\mathcal{G}}}'. \tag{2}$$

The temporal orthonormal basis $\underline{\underline{\Psi}}$ is obtained from the singular-value decomposition (SVD) of $\underline{\underline{\mathcal{C}}}$

$$\underline{\underline{\mathcal{C}}} = \underline{\underline{\Psi}}\,\underline{\underline{\Sigma}}^2\,\underline{\underline{\Psi}}', \tag{3}$$

where $\underline{\underline{\Sigma}}^2$ is a diagonal matrix containing the $n_\mathrm{s}$ (squared) singular values $\sigma_\mathrm{i}$ of $\underline{\underline{\mathcal{G}}}$.

The spatial basis $\underline{\underline{\Phi}}$ can be extracted using the original snapshot matrix:

$$\underline{\underline{\Phi}} = (\underline{\underline{\Sigma}}^{-1}\,\underline{\underline{\Psi}}'\,\underline{\underline{\mathcal{G}}})'. \tag{4}$$

POD is used to decompose the flow fields according to a spatial and a temporal basis. The POD spatial modes are sorted in terms of their contribution $\sigma_\mathrm{i}^2$ to the total velocity and Nusselt-number variance, respectively, allowing to estimate their relative importance in the heat-transfer and flow field. The spatial modes reported in the following represent an orthonormal basis and are presented in form of contour plots ranging from the minimum local values (represented in blue in the contour plots) to the maximum local value (represented in red).

Once the temporal and spatial orthonormal basis have been calculated, the fluctuating part of the field $g(\vec{x},t)$ can be expressed in terms of its modes as:

$$g(\vec{x},t) = \sum_{i=1}^{n_\mathrm{m}} \psi_\mathrm{i}(t)\sigma_\mathrm{i}\phi_\mathrm{i}(\vec{x}) \tag{5}$$

where $\psi_\mathrm{i}$, and $\phi_\mathrm{i}$ represent the $i^{th}$ temporal and spatial modes, contained respectively in the columns of $\underline{\underline{\Psi}}$ and $\underline{\underline{\Phi}}$ and $n_\mathrm{m}$ is the rank of the dataset used for the decomposition. It has to be remarked that, since $g(\vec{x},t)$ is a zero-mean quantity the temporal modes also have zero mean. The features represented by the spatial modes $\phi_\mathrm{i}$ (or by their combination) will depend on the sign of $\psi_\mathrm{i}(t)$.

## 3. Flow and heat transfer average quantities and statistics

In this section the flow field and heat transfer statistics are introduced and compared with the literature to build up a reference for subsequent discussion on the modal decomposition. Time-averaged wall-Nusselt-number distributions and flow fields are reported in Figures 2 and 3, respectively. The portion of the PIV fields covered by the rib and by its shadow is blanked; blanking is applied also on the area affected by the presence of the rib in the IR measurements and the Nusselt number profiles start at $x/L$=0.5 since upstream points are partially corrupted.

The heat-transfer enhancing effect caused by the introduction of an obstacle in a TBL is observed clearly in Figure 2a) which reports the spanwise-averaged Nusselt-number distribution along the streamwise direction. To better characterize the heat-transfer enhancement, the ratio between the Nusselt number in the configurations with rib and the clean configuration, $Nu_0$, is reported in Figure 2b). The maximum Nusselt number is augmented significantly, up to 60%, due to the interaction between the rib and the incoming turbulent flow. However, as expected, a recirculation region appears in the wake of the obstacle (Figure 3). This recirculation region is characterized by a low velocity magnitude, which in turn causes a reduction in the convective heat-transfer coefficient, leading to the presence of a hot spot downstream of the rib. Moreover, further downstream, due to the increased shear and Reynolds stresses caused by the introduction of an obstacle in the flow, there is a higher velocity defect in its wake when compared to the clean boundary-layer case. This dissipation caused by the increased shear leads to a higher drag, which is translated into pressure losses in the heat exchange systems in which the obstacles are used thus should be minimized.

The time-averaged flow field for the wall-attached rib case is reported in Figure 3b). As mentioned before, the obstacle leads to flow separation just downstream of it. Moreover, due to the asymmetry induced by the presence of the wall, the recirculation region extends up to 5 heights behind the obstacle. This causes the presence of a large hot-spot just after the obstacle, followed by an heat-transfer enhancement region (compared to the clean TBL case), caused by the reattachment of the flow.

In order to prevent the creation of an elongated recirculation/hot-spot region, a simple, but efficient, solution is that of introducing a gap between the wall and the obstacle. The effect in terms of heat transfer and flow organization can be seen in Figure 2 and 3c) and d), respectively. A wall-jet issues from the gap due to the difference in pressure between the front and back faces of the obstacle. The jet interacts with the recirculation bubble, 'lifting' it away from the wall and reducing its length. In terms of the convective heat transfer, the jet leads to a reduction in intensity of the hot spot region downstream of the obstacle. In the case where $H/L$=0.25, the jet is actually creating a region of high heat-transfer enhancement extending up to 1 rib-height from the obstacle's back-side. At this point, the jet momentum is dissipated in the low-speed flow and a hot spot appears. However, the streamwise length of the hot spot (only about 1 obstacle height, compared to 3 in the wall-attached case) and its penalty on the heat transfer are much lower than in the case in which the obstacle is directly attached onto the wall. The gap also affects the position of the minimum heat-transfer point: for the case with $H/L = 0.25$ the minimum is located at $x/L \approx 1.5$, while for $H/L$=0.5 the minimum occurs at $x/L \approx 1$.

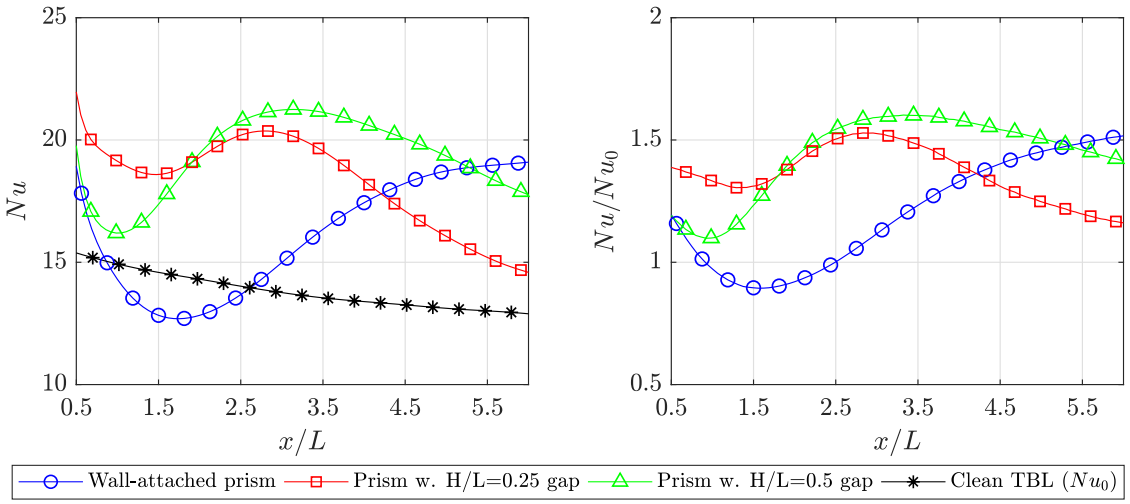


Figure 2: Time-averaged a) Nusselt-number distributions, and b) Nusselt-number augmentation distributions (markers are placed every 5 measurement points).

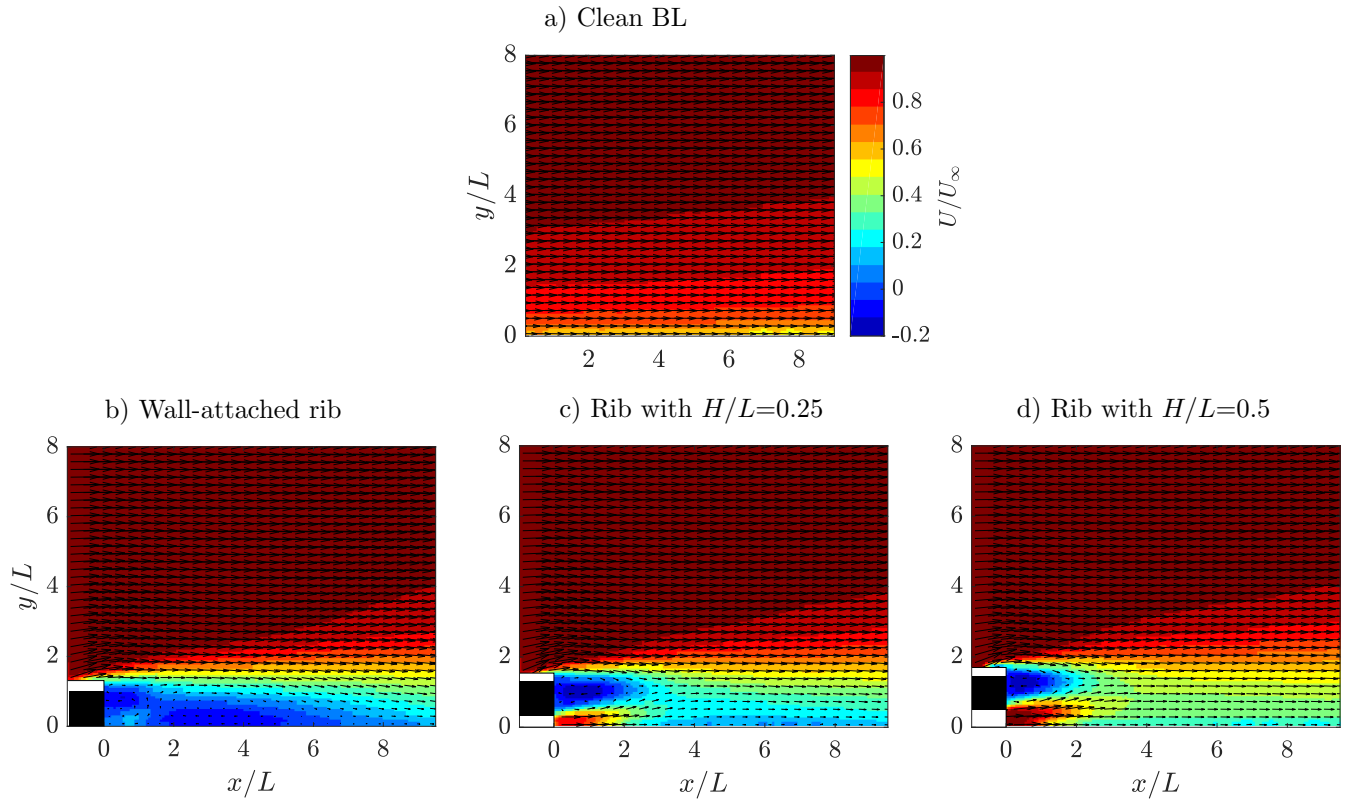


Figure 3: Time-averaged flow fields for the a) clean boundary layer, b) wall-attached rib, c) rib with $H/L$=0.25 and d) rib with $H/L$=0.5.

Moreover, the 'localization' of the recirculation region allows for a quicker reattachment of the flow, which in turn produces a region of maximum heat-transfer augmentation. As can be seen in Figure 3, introducing a bigger gap allows for high-momentum penetration in the region past the obstacle. The high difference in momentum between the jet and the recirculation region results in a reduction of the recirculation bubble streamwise extent. This shortening promotes an earlier reattachment of the flow. The reattaching flow impinges onto the wall, causing the appearance of regions of $Nu$ maximum at $x/L \approx 3$, which increases in intensity with increasing gap distance. The heat-transfer past the reattachment point is similarly increased for increasing gap distance.

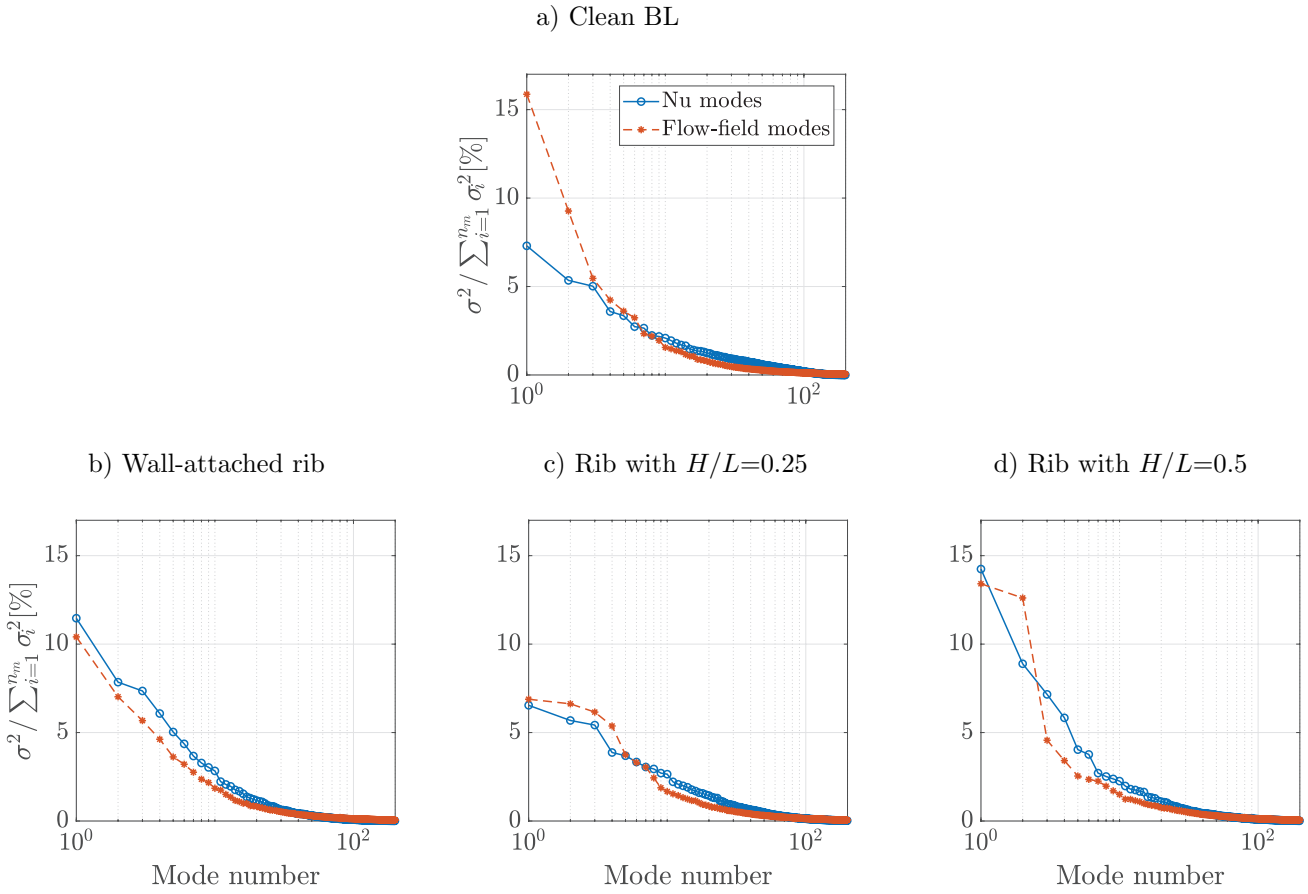


Figure 4: Relative weight (in % contribution to the total) of the POD modes for both the Nusselt-number distribution and flow field for the a) clean boundary layer, b) wall-attached rib, c) rib with $H/L$=0.25 and d) rib with $H/L$=0.5.

The ensemble-averaged $Nu$ and streamwise velocity contour maps in the near-field of the rib (up to 6 heights downstream from it) are in qualitative agreement with the results of He et al. [20]. Similar heat-transfer enhancement patterns and wake organizations for the different gap ($H/L$) values are observed. The discrepancies between the present work and Ref. [20] occur immediately downstream of the obstacle for both the wall-attached rib configuration and for the configuration with $H/L = 0.25$. This difference, apart of the different Reynolds number, has to be ascribed to the different value of $L/\delta_{99}$ employed in the two studies (equal to 0.25 and 0.5, respectively).

The different value of $L/\delta_{99}$ has a significant effect for the configuration with $H/L = 0.25$. This difference results in a value of $H/\delta_{99} = 0.0625$ (compared with $H/\delta_{99} = 0.125$ in Ref. [20]). Considering a typical profile for a developed TBL over a flat plate (see, Ref. [27]), in the present work the gap is completely immersed in the overlap region, while in Ref. [20] the gap spans from the wall and out of the logarithmic region of the BL. Therefore, the momentum flux across the gap, which produces a jet, is much lower in the present work, providing a much weaker enhancement of the heat transfer just downstream of the obstacle (which, instead, in Ref. [20] is reported to be maximum immediately after the obstacle). In the present study, the maximum of the Nusselt number can be found around 2 heights behind the obstacle (see Figure 2), coinciding with the spot in which the jet and the shedding layer interact more strongly (as it can be seen in the mean flow plot Fig. 3 and more clearly in the POD modes of the flow field in the next paragraph).

For what concerns the value of the Nusselt number immediately downstream of the obstacle for the wall-attached rib configuration, Ref. [20] reports a minimum while in our work this minimum is found at a distance of $1.5L$ downstream of the rib (see Fig. 2), i.e. in the middle of the recirculation region reported in Fig. 3. Such a discrepancy is typically encountered in the literature (see, e.g. Ref. [17, 46]) and might be ascribed again to different values of the rib to boundary layer height $L/\delta_{99}$, affecting the kinetic energy content of the recirculation region.

## 4. Modal decomposition

As in the case of the time-averaged fields, it is convenient to start the analysis by first looking at the effect

on the flow caused by the introduction of an obstacle in the TBL. In order to do so, the eigenspectra and the spatial modes of the velocity disturbance component ($\vec{u}(\vec{x},t)$) will be analyzed. The sum of the squares of the singular values of the snapshot matrix represent the variance of the in-plane velocity fluctuations ($\overline{u'^2+v'^2}$), therefore, the relative weight of each mode, given by its square singular value, is an estimation of the contribution of a certain spatial mode to the flow in-plane turbulent kinetic energy (TKE).

The percent contribution of each of the modes to the TKE is reported in Figure 4 for the velocity fields modes in the streamwise/wall-normal planes. In agreement with the literature [47, 48], for the boundary layer without ribs, the bulk of the turbulent kinetic energy is contained in the first four velocity POD modes which represent more than 30% of the turbulent kinetic energy content. These modes are reported in Figure 5 and are shown to be representative of large-scale sweeps/ejections, creating streaks with large streamwise wavelengths. A detailed discussion about the organization of the modes in zero- and adverse-pressure-gradient turbulent boundary layer is reported in Refs. [47, 48].

The introduction of the rib drastically alters the characteristic flow features and their relative importance in the POD spectrum. The spectral distribution strongly depends on the gap between the rib and the wall. For the wall-attached rib case the variance content rapidly decreases with increasing mode number, while wall-proximity rib cases are characterized by a similar variance content in the first two modes. Due to the optimality property of the POD, the mode singular values have to decrease monotonically, generally leading to a power-law distribution in the POD spectrum; a similar variance content between different modes indicates that these modes are strongly coupled, being orthogonal components of a traveling wave, i.e. they are part of the same turbulent coherent structure (see e.g. Ref. [24]). The mode coupling can be better spotted by visual inspection of the spatial modes reported in Figure 5. For the wall-attached rib case (Figure 5a), the first four POD modes seem to be uncoupled, i.e. there is no clear pattern in the shape and position of the features of different modes. The vortical features contained in these modes capture the effect of the Kelvin-Helmholtz instabilities, resulting in span-wise oriented eddies which characterize the outer region of the rib wake. When a gap is introduced between the rib and the wall, the mode coupling can be observed as predicted by the POD spectrum: in the largest gap case ($H/L$=0.5), the two first modes are clearly coupled, both in terms of their spectral contribution (see Figure 4d) and in terms of their spatial bases (see Figure 5d) which have the same spatial wavelength and differ mostly for a spatial shift between them. In this case, the gap is large enough to enable the appearance of a clear von Kármán vortex shedding in the first two modes, even if strongly perturbed by the presence of the high-momentum jet. Conversely, for $H/L$=0.25 (Figure 5c), the first three modes are strongly interconnected, as suggested by their spectral contribution (see Figure 5c). These first three modes do not model a clearly defined instability in the flow, but rather correspond to a mixed instability (including characteristics of both von Kármán and Kelvin-Helmholtz instabilities). This result is consistent with the reduced momentum flux through the gap due to the low value $H/\delta_{99}$. The near-wall interaction between the jet passing through the gap and the eddies shed from the rib is maximum at approximately at a distance of $2L$ downstream of the rib, in correspondence of the local $Nu$ maximum identified in Figure 2.

According to the previous analysis, the flow field downstream of the rib is characterized by a von Kármán shedding (gathering $\sim$ 27% of the TKE in the first 2 modes) for $H/L$=0.5 and by a pure Kelvin-Helmholtz instability (gathering $\sim$ 20% of the TKE in the first 3 modes) in the shear layer released from the top of the obstacle for the wall-attached rib. The case with $H/L$=0.25, instead, is less dominated by a single instability (the first 3 modes vary highly in their TKE contribution, gathering $\sim$ 22% of the TKE combined), resulting therefore in a less coherent flow. These effects are consistent with the picture of a transition from a flow field dominated by Kelvin-Helmholtz instabilities on the edges of the recirculation region (wall-attached configuration) to a regime dominated by von Kármán vortex shedding in the rib wake (with the rib detached from the wall), thus increasing the energetic content of the modes associated with these instabilities. Due to the increase of the gap between the rib and the wall, the von Kármán vortex shedding becomes more prominent and the modes acquire more coherence.

Lastly, the effect of the gap, apart from inducing a transition from a Kelvin-Helmholtz to a von Kármán vortex-dominated wake, can be observed in the third and fourth modes of the configurations with a gap (c and d in Figure 5). These modes represent the complex effect that the wall-jet has on the obstacle's wake: the jet issued from the gap interacts with the wake instabilities, producing a flapping of the jet itself and affecting the recirculation region, the wake shedding and the reattaching flow. These structures correspond to a flapping mode of the high-momentum jet issued from the gap, which is in fact affecting the obstacle wake topology.

The percent contribution of the $Nu$ modes to the total Nusselt-number variance is reported in Figure 4. Although the modes represent phenomena with zero mean, the $Nu$ variance content identifies the mechanisms through which turbulent transport occurs instantaneously; a discussion of the modes of the Nusselt-number variance thus allows to identify and hierarchically order the coherent events responsible for the turbulent thermal transport. Apart from the clean BL case, the trend of the variance content in the POD eigenspectrum is rather similar between flow-field and Nusselt-number modes, especially for the most relevant modes in terms of variance; the only relevant systematic difference between the two POD spec-

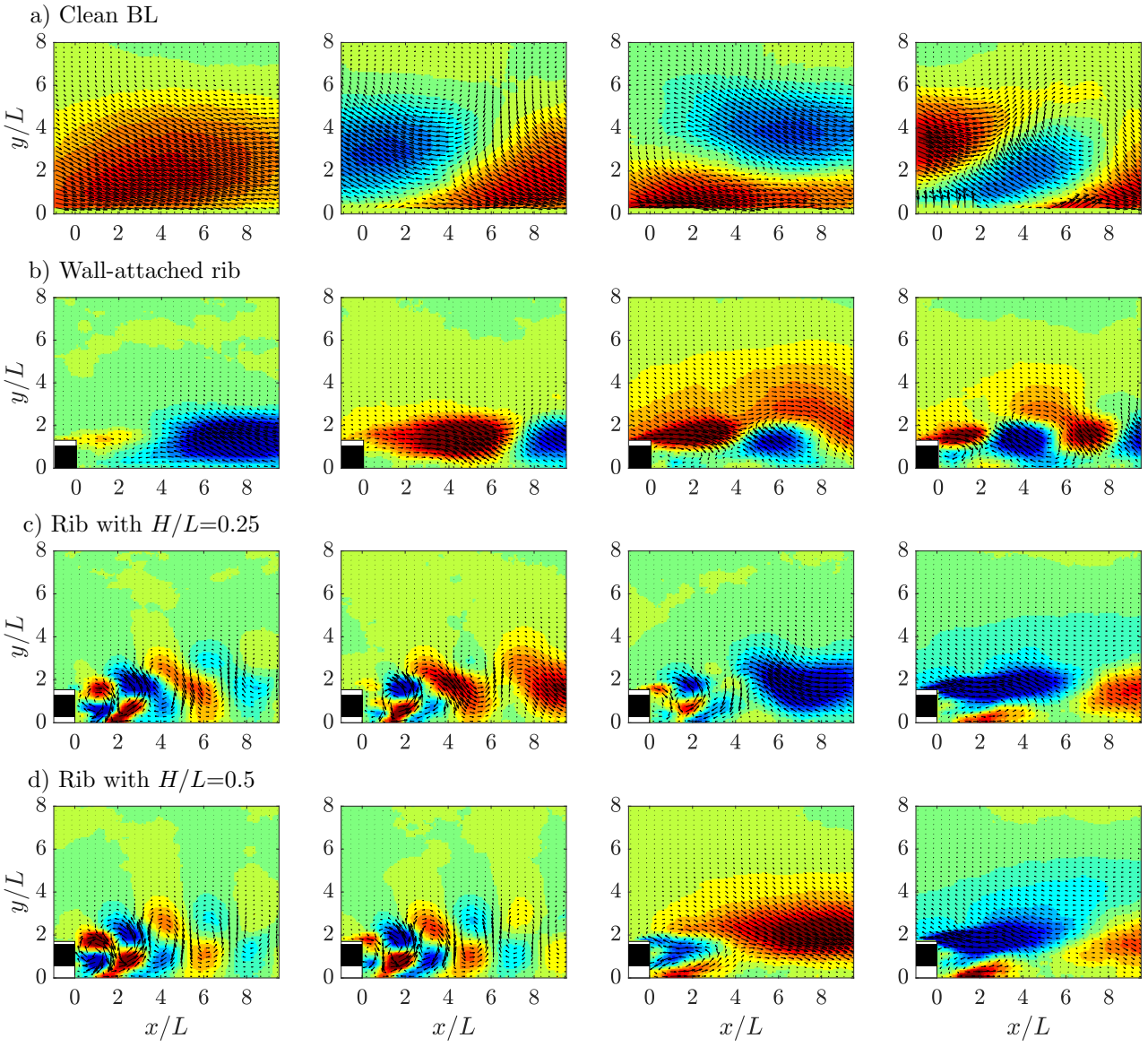


Figure 5: First four flow-field modes for the a) clean boundary layer, b) wall-attached rib, c) rib with $H/L$=0.25 and d) rib with $H/L$=0.5: contour of normalized streamwise velocity fluctuations with superimposed vector arrows.

tra is that the Nusselt-number variance is more spread-out than the turbulent kinetic energy, possibly due to a higher random error content in the measurement of the former quantity (see [8] for further insight on the noise effect in the POD spectrum). This close relation between both spectra suggests that the turbulent convective heat transfer is driven by the most energetic and coherent near-wall features. This aspect supports the idea that a high coherence of the near-wall flow features, and thus a high coherence of the associated Nusselt-number modes, has an effect also on the mean $Nu$ distribution. In fact, for a wall-attached rib the shear-layer instabilities are highly coherent (with a significantly high variance content in the first mode; cf. Figure 4b)) which leads to higher $Nu$ values downstream of the obstacle. Even better performances are achieved for $H/L$=0.5 where the Kelvin-Helmholtz instability is disrupted (resulting in a minor augmentation far downstream) but a highly coherent von Kármán shedding is present (resulting in highly coherent near-wall features, as shown in Figures 4d) and 5), with a consequent augmentation in the region where the turbulent structures are impacting the wall ($0-4L$ downstream of obstacle, as shown in Figures 2d) and 5d)). For the case with a gap of $0.25L$, the flow is characterized by a balance between von Kármán shedding and pure Kelvin-Helmholtz instability: the modes experience a smaller variance content (as evident from Figure 4c)) which leads to a lower $Nu$ augmentation far downstream with respect to the wall-attached rib, and lower augmentation just after the rib with respect to the case with $H/L$=0.5.

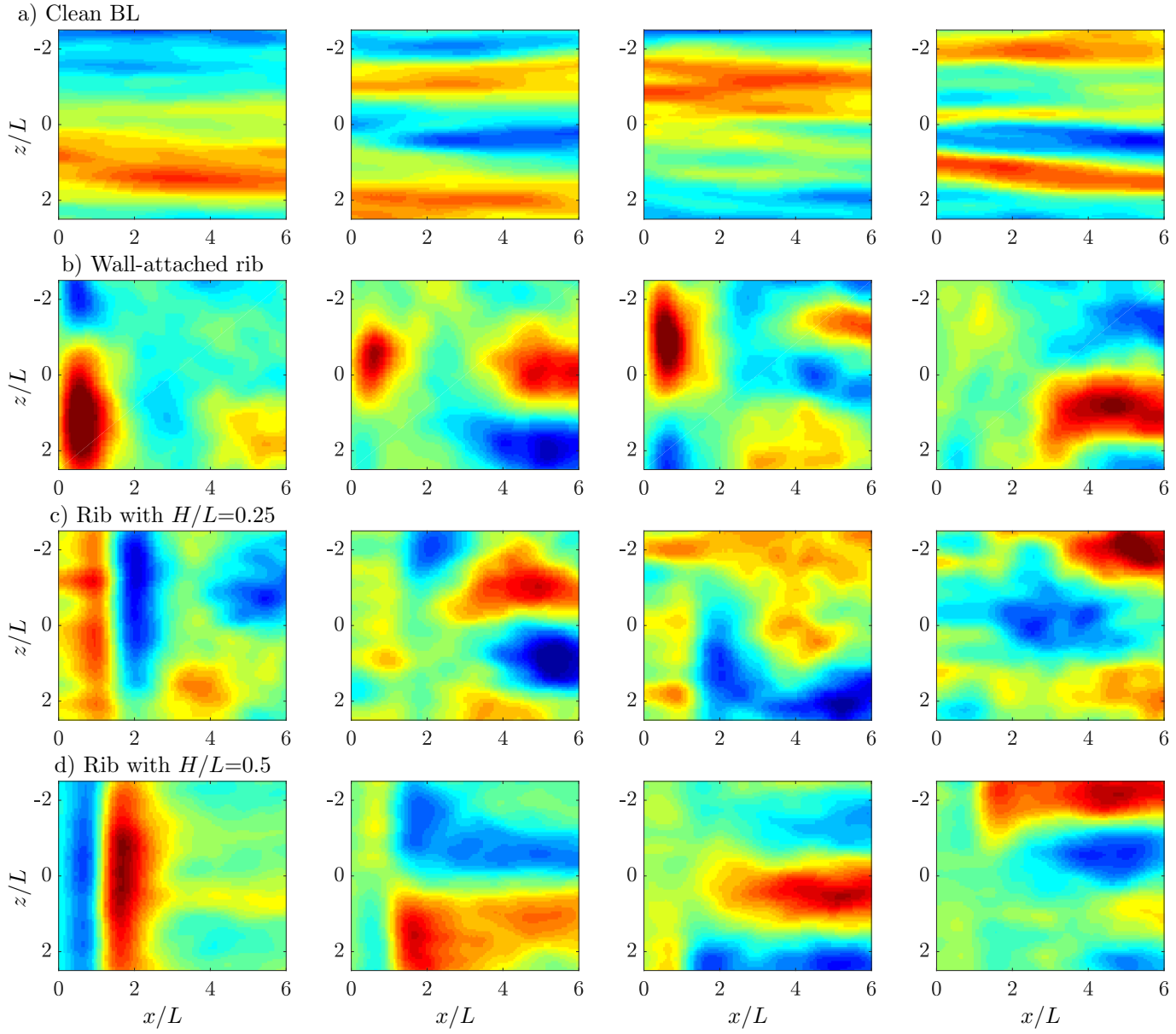


Figure 6: First four spatial modes of the unsteady convective heat transfer ($Nu'$) obtained using POD for the a) clean boundary layer, b) wall-attached rib, c) rib with $H/L$=0.25 and d) rib with $H/L$=0.5.

The modes spatial organization in the clean turbulent boundary layer is characterized by low/high Nusselt number streamwise streaks (Figure 6a)). In fact, due to the statistical homogeneity, the POD modes correspond actually to Fourier modes in the spanwise direction (see, e.g. Ref. [49]), with the lower frequency harmonics giving the higher contribution to the Nusselt-number variance spectra (Figure 4). The streaky pattern is directly related to the turbulent coherent structures observed in the velocity POD modes: the ejections/sweeps of the flow are caused by the presence of counter-rotating streamwise vortex pairs [50]. These vortices induce high-momentum streaks on a region corresponding to half a spanwise wavelength by displacing high momentum flow from the upper regions of the boundary layer towards the wall, and causing the opposite effect on the other half spanwise wavelength. This has the effect of creating periodic high- and low-speed streaks in the near-wall region, which lead to the periodic streaky pattern observed in all the modes of $Nu$ in the clean TBL configuration.

The introduction of the ribs disturbs the formation of the streaky pattern observed in the $Nu$ modes of the clean boundary layer; the rib acts as a vortex generator, producing spanwise oriented vorticity and disrupting the action of the large-scale coherent structures responsible for the presence of the streaks at the wall. However, sufficiently downstream of the rib, when the obstacle's effect on the flow is diminished (i.e. when the flow reattaches), the peri-

odicity in the spanwise direction is recovered and the variance of the convective heat transfer is again dominated by a streaky pattern (with larger spanwise wavelength with respect to the clean boundary layer case). Streaky patterns are evident starting from the second mode, revealing that the relative contribution of these features to the Nusselt-number variance is reduced. These span-wise-periodic features are to be ascribed to the spanwise vortices developed due to the separation in the rib shear layer which evolve downstream and undergo tilting and a set of instabilities (see, e.g. the 3D cylinder wakes reported in Ref. [51]). The present measurements are not focusing on a flow region located at a large-enough downstream region to have recovered the profile of a clean boundary layer. Having well-developed span-wise eddies, however, results in much more ordered and coherent pattern than in the clean boundary layer.

The first mode is instead dominated by the spanwise thermal footprint of the spanwise-oriented vorticity (also captured by the velocity modes) right downstream of the rib. In the wall-attached rib case, the highest variance corresponds to the recirculation region, and can be related to the interaction between the recirculation and the shear-layer instabilities in the outer region of the rib wake, which causes fluctuations in the velocity close to the wall; this effect can be seen also in the first flow-field mode (Figure 5b).

The introduction of a gap between the wall and the rib produces a wall-jet, which, due to its flapping, causes fluctuations in the velocity nearby the wall and thus in the $Nu$ map. Moreover, the reduction of the size of the recirculation bubble causes an impingement of the flow shed from the top of the obstacle. The modulation between the region of maximum and minimum convective heat transfer depends on these two effects, which are clearly depicted by the velocity modes, as well as by the mean flow contour maps (Figure 3). Moreover, as mentioned before, the larger gap ($H/L$=0.5) allows a transition from a less temporally-coherent Kelvin-Helmholtz instability to a more temporally-coherent von Kármán shedding, which results in a more periodic and organized distribution of the Nusselt-number variance. The spanwise sinusoidal variation of the Nusselt-number modes characteristics of the $H/L$=0.5 case might be ascribed to the three dimensionality in the rib turbulent wake which is well assessed for cylinders [51].

The present results support a picture of direct relation between the coherence of near-wall flow features and heat transfer augmentation, providing a statistical evidence for the *surface renewal* concept introduced by Kataoka et al. for impinging jets [52]. Large-scale coherent eddies are extremely efficient in improving scalar transport whenever they are located in proximity of the wall.

This direct relation between the near-wall eddies coherence (given by their eigenvalue weight) and the convective heat transfer augmentation suggests that high coherence of near-wall turbulent structures should be sought after when designing vortex generators for heat-transfer augmentation purposes.

## 5. Conclusions

In this work the combined use of modal decomposition on flow fields and convective heat transfer distributions is explored. The objective is to demonstrate this approach as a method to discern flow field features which are responsible for heat transfer enhancement. For this purpose, an application to the case of square wall-proximity ribs is illustrated. The gap from the wall is changed in order to obtain different flow field and heat transfer configurations to test the proposed technique.

The flow-field modal analysis, as well known from the literature, highlighted a significantly different flow organization in the flow past the ribs depending on the rib distance from the wall. A von Kármán shedding has been observed for the case with gap ratio $H/L$=0.5, while a Kelvin-Helmholtz instability occurs for the wall-attached rib case.

The gap ratio $H/L$=0.5 attains the best performance in terms of convective heat transfer within the tested configurations. This result is in disagreement with respect to the findings reported in Ref. [20] in which a bigger rib-to-boundary-layer-thickness ratio was employed. The performance enhancement is ascribed to the formation of a wall jet which is characterized by a flapping motion due to the von Kármán vortex shedding in the wake of the square ribs; in Ref. [20] the larger rib employed resulted in a similar momentum flux for the near wall jet produced for $H/L = 0.25$. This enhancement mechanism is reflected by both the increased energy content and spatial coherence of the main flow-field POD modes and by the increase of the variance content and coherence of the Nusselt-number spatial modes related to the wall jet flapping.

The comparison of the Nusselt-number spatial modes of the clean turbulent boundary layer configuration and of the configurations with the ribs shows a variation of the spatial pattern associated with oscillations with strong spanwise coherence, opposed to the thin elongated streaks which dominate the convective heat transfer in the clean turbulent boundary layer.

It has to be remarked that, for the case in which coherent structures generation is enhanced (for instance $H/L$=0.5), the modal description of the Nusselt number fluctuations becomes more compact, i.e. more energy is contained in the first modes. This is coupled with an overall enhanced average Nusselt-number distribution, thus demonstrating that increased coherence of near-wall eddies enhances the wall convective heat transfer.

It can be concluded that the combined use of modal decomposition on convective heat transfer and flow field modes is a promising avenue for the understanding of heat transfer mechanisms in turbulent flow. If a clear relation between POD modes of the instantaneous Nusselt number maps and flow field POD modes is observed, than the

coherent structures present in the modes are those responsible for the heat transfer enhancement. Otherwise, the coherent structures identified by the flow field POD modes, but not directly interpreted also in terms of footprint on the heat transfer POD modes, are not active in heat transfer enhancement, even if highly energetic.

## Acknowledgments

This work has been partially supported by the Grant DPI2016-79401-R funded by the Spanish State Research Agency (SRA) and European Regional Development Fund (ERDF).

## References

[1] J.-C. Han, S. Dutta, S. Ekkad, Gas turbine heat transfer and cooling technology, CRC Press, 2012.

[2] S. V. Garimella, L.-T. Yeh, T. Persoons, Thermal management challenges in telecommunication systems and data centers, IEEE Trans. Compon. Packaging Manuf. Technol. 2 (2012) 1307–1316.

[3] T. L. Bergman, F. P. Incropera, D. P. DeWitt, A. S. Lavine, Fundamentals of heat and mass transfer, John Wiley & Sons, 2011.

[4] G. Berkooz, P. Holmes, J. L. Lumley, The proper orthogonal decomposition in the analysis of turbulent flows, Annu. Rev. Fluid Mech. 25 (1) (1993) 539–575.

[5] R. Gurka, A. Liberzon, G. Hetsroni, Detecting coherent patterns in a flume by using PIV and IR imaging techniques, Exp. Fluids 37 (2004) 230–236.

[6] H. Nakamura, S. Yamada, Quantitative evaluation of spatio-temporal heat transfer to a turbulent air flow using a heated thin-foil, Int. J. Heat Mass Transfer 64 (2013) 892–902.

[7] S. Yamada, H. Nakamura, Construction of 2D-3C PIV and high-speed infrared thermography combined system for simultaneous measurement of flow and thermal fluctuations over a backward facing step, Int. J. Heat Fluid Flow 61 (2016) 174–182.

[8] M. Raiola, C. S. Greco, M. Contino, S. Discetti, A. Ianiro, Towards enabling time-resolved measurements of turbulent convective heat transfer maps with IR thermography and a heated thin foil, Int. J. Heat Mass Transfer 108 (2017) 199–209.

[9] A. Antoranz, A. Ianiro, O. Flores, M. García-Villalba, Extended proper orthogonal decomposition of non-homogeneous thermal fields in a turbulent pipe flow, Int. J. Heat Mass Transfer 118 (2018) 1264–1275.

[10] K.-Q. Xia, How heat transfer efficiencies in turbulent thermal convection depend on internal flow modes, J. Fluid Mech. 676 (2011) 1–4.

[11] S. Weiss, G. Ahlers, Turbulent Rayleigh–Bénard convection in a cylindrical container with aspect ratio $\Gamma = 0.50$ and Prandtl number $Pr = 4.38$, J. Fluid Mech. 676 (2011) 5–40.

[12] J. Borée, Extended proper orthogonal decomposition: a tool to analyse correlated events in turbulent flows, Exp. Fluids 35 (2003) 188–192.

[13] R. Webb, E. Eckert, R. Goldstein, Heat transfer and friction in tubes with repeated-rib roughness, Int. J. Heat Mass Transfer 14 (1971) 601–617.

[14] T.-M. Liou, W.-B. Wang, Laser holographic interferometry study of developing heat transfer in a duct with a detached rib array, Int. J. Heat Mass Transfer 38 (1995) 91–100.

[15] T. Astarita, G. Cardone, Convective heat transfer in a square channel with angled ribs on two opposite walls, Exp. Fluids 34 (2003) 625–634.

[16] Y. I. Smulsky, V. I. Terekhov, N. I. Yarygina, Heat transfer in turbulent separated flow behind a rib on the surface of square channel at different orientation angles relative to flow direction, Int. J. Heat Mass Transfer 55 (2012) 726–733.

[17] R. T. Kukreja, S. C. Lau, R. D. McMillin, Local heat/mass transfer distribution in a square channel with full and v-shaped ribs, Int. J. Heat Mass Transfer 36 (1993) 2013–2020.

[18] S. Leonardi, P. Orlandi, L. Djenidi, R. Antonia, Heat transfer in a turbulent channel flow with square bars or circular rods on one wall, J. Fluid Mech. 776 (2015) 512–530.

[19] S. M. Islam, K. Haga, M. Kaminaga, R. Hino, M. Monde, Experimental analysis of turbulent flow structure in a fully developed rib-roughened rectangular channel with piv, Exp. Fluids 33 (2002) 296–306.

[20] C. He, Y. Liu, D. Peng, S. Yavuzkurt, Measurement of flow structures and heat transfer behind a wall-proximity square rib using TSP, PIV and split-fiber film, Exp. Fluids 57 (2016) 165.

[21] F. Mallor, C. Sanmiguel Vila, A. Ianiro, S. Discetti, Wall-mounted perforated cubes in a boundary layer: Local heat transfer enhancement and control, Int. J. Heat Mass Transfer 117 (2018) 498–507.

[22] Y. Liu, F. Ke, H. Sung, Unsteady separated and reattaching turbulent flow over a two-dimensional square rib, J. Fluids Struct. 24 (2008) 366–381.

[23] I. Mayo, T. Arts, L. Y. Gicquel, The three-dimensional flow field and heat transfer in a rib-roughened channel at large rotation numbers, Int. J. Heat Mass Transfer 123 (2018) 848–866.

[24] M. Raiola, A. Ianiro, S. Discetti, Wake of tandem cylinders near a wall, Exp. Therm Fluid Sci. 78 (2016) 354–369.

[25] J. Westerweel, G. E. Elsinga, R. J. Adrian, Particle image velocimetry for complex and turbulent flows, Annu. Rev. Fluid Mech. 45 (2013) 409–436.

[26] P. Schlatter, R. Örlü, Turbulent boundary layers at moderate Reynolds numbers: inflow length and tripping effects, J. Fluid Mech. 710 (2012) 534.

[27] C. Sanmiguel Vila, R. Vinuesa, S. Discetti, A. Ianiro, P. Schlatter, R. Örlü, On the identification of well-behaved turbulent boundary layers, J. Fluid Mech. 822 (2017) 109–138.

[28] N. Agüera, G. Cafiero, T. Astarita, S. Discetti, Ensemble 3D PTV for high resolution turbulent statistics, Meas. Sci. Technol. 27 (12) (2016) 124011.

[29] K. A. Chauhan, P. A. Monkewitz, H. M. Nagib, Criteria for assessing experiments in zero pressure gradient boundary layers, Fluid Dyn. Res. 41 (2009) 021404.

[30] R. Örlü, J. H. M. Fransson, P. H. Alfredsson, On near wall measurements of wall bounded flows—The necessity of an accurate determination of the wall position, Prog. Aerosp. Sci. 46 (8) (2010) 353–387.

[31] G. M. Carlomagno, G. Cardone, Infrared thermography for convective heat transfer measurements, Exp. Fluids 49 (2010) 1187–1218.

[32] H. Nakamura, Frequency response and spatial resolution of a thin foil for heat transfer measurements using infrared thermography, Int. J. Heat Mass Transfer 52 (2009) 5040–5045.

[33] A. F. M. Torre, A. Ianiro, S. Discetti, G. M. Carlomagno, Evaluation of anisotropic tangential conduction in printed-circuit-board heated-thin-foil heat flux sensors, Int. J. Heat Mass Transfer 127 (2018) 1138–1146.

[34] S. Discetti, R. J. Adrian, High accuracy measurement of magnification for monocular PIV, Meas. Sci. Technol. 23 (11) (2012) 117001.

[35] M. Mendez, M. Raiola, A. Masullo, S. Discetti, A. Ianiro, R. Theunissen, J.-M. Buchlin, POD-based background removal for particle image velocimetry, Exp. Therm. Fluid Sci. 80 (2017) 181–192.

[36] C. E. Willert, M. Gharib, Digital particle image velocimetry, Exp. Fluids 10 (4) (1991) 181–193.

[37] J. Soria, An investigation of the near wake of a circular cylinder using a video-based digital cross-correlation particle image velocimetry technique, Exp. Therm. Fluid Sci. 12 (1996) 221–233.

[38] F. Scarano, Iterative image deformation methods in PIV, Meas. Sci. Technol. 13 (2001) R1–R13.

[39] T. Astarita, G. Cardone, Analysis of interpolation schemes for image deformation methods in PIV, Exp. Fluids 38 (2005) 233–243.

[40] T. Astarita, Analysis of interpolation schemes for image deformation methods in PIV: effect of noise on the accuracy and spatial resolution, Exp. Fluids 40 (2006) 977–987.
[41] J. Westerweel, F. Scarano, Universal outlier detection for PIV data, Exp. Fluids 39 (2005) 1096–1100.
[42] R. J. Moffat, Describing the uncertainties in experimental results, Exp. Therm. Fluid Sci. 1 (1988) 3–17.
[43] C. S. Greco, G. Paolillo, A. Ianiro, G. Cardone, L. de Luca, Effects of the stroke length and nozzle-to-plate distance on synthetic jet impingement heat transfer, Int. J. Heat Mass Transfer 117 (2018) 1019–1031.
[44] L. Sirovich, Turbulence and the dynamics of coherent structures. I. Coherent structures, Q. Appl. Math. 45 (1987) 561–571.
[45] P. Holmes, J. L. Lumley, G. Berkooz, C. W. Rowley, Turbulence, coherent structures, dynamical systems and symmetry, Cambridge University Press, 2012.
[46] T.-M. Liou, J.-J. Hwang, Effect of ridge shapes on turbulent heat transfer and friction in a rectangular channel, Int. J. Heat Mass Transfer 36 (1993) 931–940.
[47] C. Sanmiguel Vila, R. Örlü, R. Vinuesa, P. Schlatter, A. Ianiro, S. Discetti, Adverse-pressure-gradient effects on turbulent boundary layers: Statistics and flow-field organization, Flow Turbul. Combust. 99 (2017) 589–612.
[48] Y. Wu, A study of energetic large-scale structures in turbulent boundary layer, Phys. Fluids 26 (2014) 045113.
[49] M. Tutkun, W. K. George, Lumley decomposition of turbulent boundary layer at high Reynolds numbers, Phys. Fluids 29 (2017) 020707.
[50] J. Jiménez, Coherent structures in wall-bounded turbulence, J. Fluid Mech. 842 (2018) P1–100.
[51] F. Scarano, C. Poelma, Three-dimensional vorticity patterns of cylinder wakes, Exp. Fluids 47 (2009) 69.
[52] K. Kataoka, M. Suguro, H. Degawa, K. Maruo, I. Mihata, The effect of surface renewal due to largescale eddies on jet impingement heat transfer, Int. J. Heat Mass Transfer 30 (1987) 559–567.